Monthly Notices
of the
ROYAL ASTRONOMICAL SOCIETY

Mon. Not. R. Astron. Soc. **414,** 2424–2435 (2011) doi:10.1111/j.1365-2966.2011.18562.x

Dust-correlated cm wavelength continuum emission from translucent clouds ζ Oph and LDN 1780

M. Vidal,[1,2⋆] S. Casassus,[2,3] C. Dickinson,[1] A. N. Witt,[4] P. Castellanos,[2] R. D. Davies,[1] R. J. Davis,[1] G. Cabrera,[2] K. Cleary,[5] J. R. Allison,[6] J. R. Bond,[7] L. Bronfman,[2] R. Bustos,[2,8] M. E. Jones,[6] R. Paladini,[9] T. J. Pearson,[5] A. C. S. Readhead,[5] R. Reeves,[10] J. L. Sievers[7] and A. C. Taylor[6]

[1]*Jodrell Bank Centre for Astrophysics, Alan Turing Building, School of Physics and Astronomy, The University of Manchester, Oxford Road, Manchester M13 9PL*
[2]*Departamento de Astronomía, Universidad de Chile, Casilla 36-D, Santiago, Chile*
[3]*Observatoire de Paris, LUTH and Université Denis Diderot, Place J. Janssen, 92190 Meudon, France*
[4]*Ritter Astrophysical Research Center, University of Toledo, Toledo, OH 43606, USA*
[5]*Cahill Center for Astronomy and Astrophysics, Mail Code 249-17, California Institute of Technology, Pasadena, CA 91125, USA*
[6]*Oxford Astrophysics, University of Oxford, Denys Wilkinson Building, Keble Road, Oxford OX1 3RH*
[7]*Canadian Institute for Theoretical Astrophysics, University of Toronto, Toronto, Canada*
[8]*Departamento de Astronomía, Universidad de Concepción, Casilla 160-C, Concepción, Chile*
[9]*Spitzer Science Center, 1200 East California Boulevard, Pasadena, CA 91125, USA*
[10]*Departamento de Ingeniería Eléctrica, Universidad de Concepción, Concepción, Chile*

Accepted 2011 February 17. Received 2011 February 17; in original form 2010 August 11

ABSTRACT

The diffuse cm wave IR-correlated signal, the 'anomalous' CMB foreground, is thought to arise in the dust in cirrus clouds. We present Cosmic Background Imager (CBI) cm wave data of two translucent clouds, ζ Oph and LDN 1780 with the aim of characterizing the anomalous emission in the translucent cloud environment.

In ζ Oph, the measured brightness at 31 GHz is 2.4σ higher than an extrapolation from 5-GHz measurements assuming a free–free spectrum on 8 arcmin scales. The SED of this cloud on angular scales of 1° is dominated by free–free emission in the cm range. In LDN 1780 we detected a 3σ excess in the SED on angular scales of 1° that can be fitted using a spinning dust model. In this cloud, there is a spatial correlation between the CBI data and IR images, which trace dust. The correlation is better with near-IR templates (*IRAS* 12 and 25 μm) than with *IRAS* 100 μm, which suggests a very small grain origin for the emission at 31 GHz.

We calculated the 31-GHz emissivities in both clouds. They are similar and have intermediate values between that of cirrus clouds and dark clouds. Nevertheless, we found an indication of an inverse relationship between emissivity and column density, which further supports the VSGs origin for the cm emission since the proportion of big relative to small grains is smaller in diffuse clouds.

Key words: radiation mechanisms: general – ISM: individual objects: LDN 1780 – ISM: individual objects: ζ Ophiuchi – radio continuum: ISM.

1 INTRODUCTION

Amongst the challenges involved in the study of cosmic microwave background (CMB) anisotropies is the subtraction of Galactic foreground emission. The detailed study of these foregrounds led to the discovery of a new radio-continuum mechanism in the diffuse interstellar medium (ISM). It was first detected by the *Cosmic Background Explorer* as a diffuse all-sky dust-correlated signal with a flat spectral index between 31 and 53 GHz (Kogut et al. 1996a,b). With ground based observations, Leitch et al. (1997) observed high Galactic latitude clouds and detected an excess at 14.5 GHz that, because of a lack of Hα emission, could not be accounted for by free–free with typical temperatures ($T \sim 10^4$K).

Different emission mechanisms have been proposed for the anomalous emission, such as spinning dust (Draine & Lazarian 1998a,b), magnetic dust (Draine & Lazarian 1999), hot

⋆E-mail: mvidal@jb.man.ac.uk

($T \sim 10^6$ K) free–free (Leitch et al. 1997) and hard synchrotron radiation (Bennett et al. 2003). To date, the evidence favours the spinning dust grain model (Finkbeiner et al. 2004; de Oliveira-Costa et al. 2004; Watson et al. 2005; Casassus et al. 2006, 2008; Castellanos et al. 2011) in which very small grains (VSGs) with a non-zero dipole moment rotating at GHz frequencies emit cm wave radiation. The emission has its peak at ∼20–40 GHz and the model predicts that it is dominated by the smallest grains, possibly polycyclic aromatic hydrocarbons (PAHs). Ysard, Miville-Deschênes & Verstraete (2010) found a correlation across the whole sky using *WMAP* data between 23-GHz maps and *IRAS* 12 μm, which supports the VSG origin for the cm wave emission.

The radio-infrared (radio-IR) correlation suggests that the 'cirrus' clouds are responsible for the anomalous emission at high Galactic latitudes. Cirrus is the large-scale filamentary structure detected by *IRAS* (Low et al. 1984). It is seen predominantly at 60 and 100 μm in the *IRAS* bands and the origin of this IR-radiation is generally ascribed to dust continuum emission with a contribution from atomic lines (e.g. O I 63 μm, Stark 1990). On shorter wavelengths (e.g. 12 μm), the emission is from PAHs subject to thermal fluctuations. The gas associated with cirrus clouds spans a wide range of physical parameters; most are atomic and some are molecular (e.g. Miville-Deschênes et al. 2002; Snow & McCall 2006). Stark et al. (1994), using a combination of absorption and emission line measurements, found H I gas temperatures in the range between 20 and >350 K. The low temperatures correspond to the coldest clumps in the clouds that represent the cores of the much more widely distributed and hotter H I gas. Cirrus clouds are pervaded by the interstellar radiation field (IRF). They have column densities $N(\mathrm{H\,I}) \approx 1\text{–}10 \times 10^{20}$ cm^{-2}, which correspond to visual extinctions of $A_\mathrm{V} \leq 1$ mag assuming a typical gas-to-dust ratio of 100. It is commonly found that these clouds are not gravitationally bound and that their kinematics are dominated by turbulence (Magnani, Blitz & Mundy 1985). Cirrus clouds are difficult to characterize because of their low column densities, and are thus not the best place to study the anomalous emission.

Local known clouds offer an opportunity to characterize the cm emission. A number of investigations have been made of these clouds: the Perseus molecular cloud (Watson et al. 2005), ρ Oph (Casassus et al. 2008), RCW 175 (Dickinson et al. 2009), LDN1111 (Ami Consortium et al. 2009), M78 (Castellanos et al. 2011), among others. Finkbeiner (2004) using *Wilkinson Microwave Anisotropy Probe (WMAP*, 23–94 GHz) and Green Bank (5,8,10 GHz) data fitted a spinning dust model to the emission from the cloud LDN1622. Casassus et al. (2006), with interferometric observations at 31 GHz of the same cloud, detected bright cm emission where no emission from any known mechanism was expected. They performed a morphological analysis and found a better cross-correlation between 31 GHz and *IRAS* 12 μm than with *IRAS* 100 μm. Watson et al. (2005) with the COSMOSOMAS experiment discovered strong emission in the frequency range 11–17 GHz in the Perseus Molecular Cloud (G159.6-18.5). In this cloud, the spectral energy distribution (SED) is well fitted by a spinning dust model. A disadvantage of these studies, in the aim of characterizing anomalous emission as a foreground to the CMB, is that the clouds already studied potentially constitute a very different phase of the ISM than the cirrus, so inferences drawn from them may not be applicable to understanding the anomalous emission from the cirrus seen at high Galactic latitudes.

In this paper we present cm wave continuum data for the translucent clouds ζ Oph and LDN 1780 acquired with the Cosmic Background Imager (CBI). Translucent clouds are interstellar clouds with some protection from the radiation field in that their extinction is in the range $A_\mathrm{V} \sim 1\text{–}4$ mag (Snow & McCall 2006). They can be understood as photodissociation regions (PDR). Within translucent clouds, carbon undergoes a transition from singly ionized into neutral atomic or molecular (CO) form. In translucent clouds, physical properties such as density and temperature, and environmental conditions, such as exposure to the IRF, are intermediate between those of dense clouds and those of transparent (cirrus) clouds. By bridging the gap in physical conditions, translucent clouds are test beds for the extrapolation of the radio/IR relative emissivities seen in dense clouds to those in cirrus.

The Lynds Dark Nebula (LDN) 1780 is a high Galactic latitude ($l = 359.^\circ0$, $b = 36.^\circ7$) translucent region at a distance of 110 ± 10 pc (Franco 1989). Ridderstad et al. (2006) found that the spatial distribution of the mid-IR emission differs significantly from the emission in the far-IR. Also, they show using IR colour ratios that there is an overabundance of PAHs and VSGs with respect to the solar neighbourhood (as tabulated in Boulanger & Perault 1988), although their result can be explained by an IRF that is overabundant in ultraviolet (UV) photons compared to the standard IRF (Witt et al. 2010). Using an optical-depth map constructed from *ISO* 200-μm emission, Ridderstad et al. (2006) found a mass of ∼18 $\mathrm{M}_\odot$ and reported no young stellar objects based on the absence of colour excess in point sources. Because of the morphological differences in the IR, this cloud is an interesting target to make a morphological comparison with the radio data, in order to determine the origin of the anomalous emission. The free–free emission from this cloud is very low, which is favourable for a study of the radio-IR correlated emission.

The cloud coincident with ζ Oph is a prototypical and well-studied translucent cloud. ζ Oph itself is an O9Vb star at a distance of 140 ± 16 pc (Perryman et al. 1997). In this line of sight, the total H-nucleus column density is fairly well determined, $N(\mathrm{H}) \sim 1.4 \times 10^{21}\mathrm{cm}^{-2}$, with 56 per cent of the nuclei in molecular form (Morton 1975). Although the observations reveal several interstellar components at different heliocentric velocities, the one at $v_\odot = -14.4\,\mathrm{km\,s}^{-1}$ contains most of the material and is referred to as the ζ Oph cloud. There have been numerous efforts to build chemical models of this cloud (Black & Dalgarno 1977; van Dishoeck & Black 1986; Viala, Roueff & Abgrall 1988). In the pioneering work of Black & Dalgarno (1977), a two-shell model is proposed to fit the observational data: a cold and denser core surrounded by a diffuse envelope. The density and temperature in these models are in the range $n = 250\text{–}2500$ cm^{-3}, $T = 20\text{–}100$ K for the core and $n = 200\text{–}500$ cm^{-3}, $T = 100\text{–}200$ K for the envelope. These conditions approach those of the cirrus cloud cores whose densities lie in the same range (Turner 1994).

The rest of the paper is organized as follows. In Section 2 we describe the data acquisition, image reconstruction and list the auxiliary data used for comparison with the CBI data. Section 3 contains a spectral and morphological analysis of both clouds. In Section 4 there is a comparison of the 31-GHz emissivity of dark, translucent and cirrus clouds. Section 5 presents our conclusions.

2 DATA

2.1 31-GHz observations

The observations at 31 GHz were carried out with the CBI1, (Padin et al. 2002), a 13 element interferometer located at an altitude of 5000 m in the Chajnantor plateau in Chile. Each antenna is 0.9 m

Table 1. Summary of observations. The coordinates are J2000 and the time quoted is the observation time on-source.

Source	Date	RA	Dec.	Time(s)
[a]ζ Oph	8/7/04	$16^{\rm h}\,37^{\rm m}\,9\overset{\rm s}{.}5$	$-10^\circ 34' 01''$	8000
[b]L1780E	13, 28/4/07	$15^{\rm h}\,40^{\rm m}\,30^{\rm s}$	$-07^\circ 14' 18''$	12 000
[c]L1780W	17, 18/4/07	$15^{\rm h}\,39^{\rm m}\,40^{\rm s}$	$-07^\circ 11' 40''$	8000

[a]Observed with CBI1.
[b]Observed with CBI2.

in diameter and the whole array is mounted on a tracking platform, which rotates in parallactic angle to provide uniform *uv* coverage. The primary beam has full-width half maximum (FWHM) of 45.2 arcmin at 31 GHz and the angular resolution is ∼8 arcmin. The receivers operate in ten frequency channels from 26 to 36 GHz. Each receiver measures either left (L) or right (R) circular polarization. The interferometer was upgraded during 2006–07 with 1.4-m dishes (CBI2) to increase temperature sensitivity (Taylor et al., in preparation). The primary beam is 28.2 arcmin FWHM at 31 GHz and the angular resolution was increased to ∼4 arcmin.

Table 1 summarizes the observations. Both clouds were observed in total intensity mode (all receivers measuring L only). ζ Oph was observed using CBI1 in a single position while LDN 1780 was observed in two different pointings: L1780E and L1780W by CBI2. The configurations of the CBI1 and CBI2 interferometers result in the (u, v) coverage shown in Fig. 1.

We reduced the data using the same routines as those used for CMB data analysis (Pearson et al. 2003; Readhead et al. 2004a,b). Integrations of 8 min on source were accompanied by a trail field, with an offset of 8 min in RA, observed at the same hour angle for the subtraction of local correlated emission (e.g. ground spillover). Flux calibration is tied to Jupiter (with a brightness temperature of 146.6 ± 0.75 K, Hill et al. 2009).

2.1.1 *Image reconstruction*

The reduced and calibrated visibilities were imaged with the CLEAN algorithm (Högbom 1974) using the DIFMAP package (Shepherd 1997). We chose natural weights in order to obtain a deeper restored image. The theoretical noise level (using natural weights, as expected from the visibility weights evaluated from the scatter of individual frames) is 4.9 mJy beam^{-1} for ζ Oph. Fig. 2 shows the CLEAN image of ζ Oph. This image was then corrected by the primary beam response of CBI1 at 31 GHz (45.2 arcmin). For LDN 1780, we obtained CLEAN images of the two fields. The estimated noise level is 4.3 mJy beam^{-1} for L1780E and 3.0 mJy beam^{-1} for L1780W. In LDN 1780W a point source, NVSS 153909-065843 (Condon et al. 1998), lies close to the NNW sector of the half-maximum contour of the CBI2 primary beam in Fig. 2. This source allowed us to fix the astrometry of the data which corresponded to an offset of 30 and 56 arcsec in RA and Dec. These shifts are consistent with the root mean square (rms) pointing accuracy of ∼0.5 arcmin. The restored CBI2 fields of LDN 1780 were then combined into the weighted mosaic shown on Fig. 2, according to the following formula: $I_{\rm M}(\mathbf{x}) = \sum_p (w_p(\mathbf{x}) I_p(\mathbf{x})/A_p(\mathbf{x}))/\sum_p w_p(\mathbf{x})$, where $w_p(\mathbf{x}) = A_p^2/\sigma_p^2$, with p the label for the pth pointing and $A_p(\mathbf{x})$ is the primary beam response.

We also used an alternative method to restore the visibilities in order to check the CLEAN reconstruction. We applied the Voronoi image reconstruction (VIR) from Cabrera, Casassus & Hitschfeld (2008), that is well suited to noisy data sets. This novel technique uses a Voronoi tessellation instead of the usual grid, and has the advantage that it is possible to use a smaller number of free parameters during the reconstruction. Moreover, this technique provides the optimal image in a Bayesian sense, so the final image is unique.

Fig. 3 shows the VIR image for LDN 1780. The point source was subtracted from the visibilities before the reconstruction. The result is visibly better because the image negatives are less pronounced than CLEAN (Fig. 2). The largest negative intensity with CLEAN is −0.007 MJy sr^{-1} whereas with VIR is −0.005 MJy sr^{-1}. The

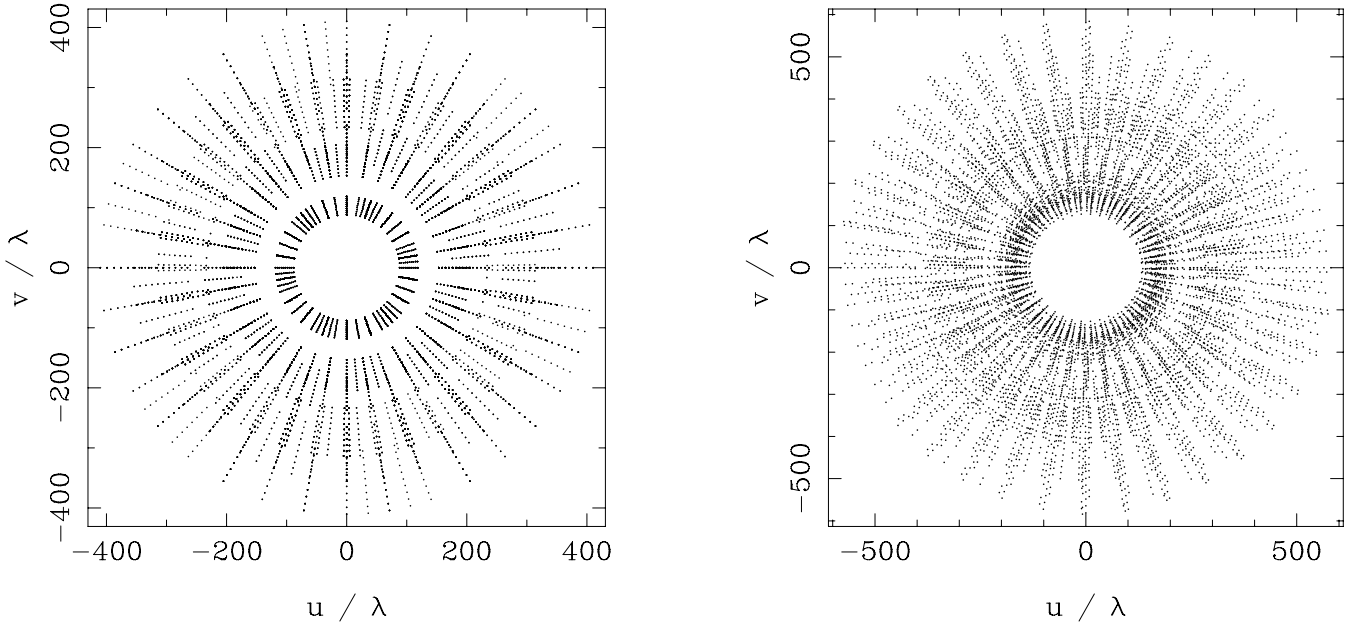

Figure 1. (u, v) coverage of the CBI1 (left) and CBI2 (right) in the configurations used for the observations of ζ Oph on the left and LDN 1780 on the right. Axes are in units of wavelength (λ).

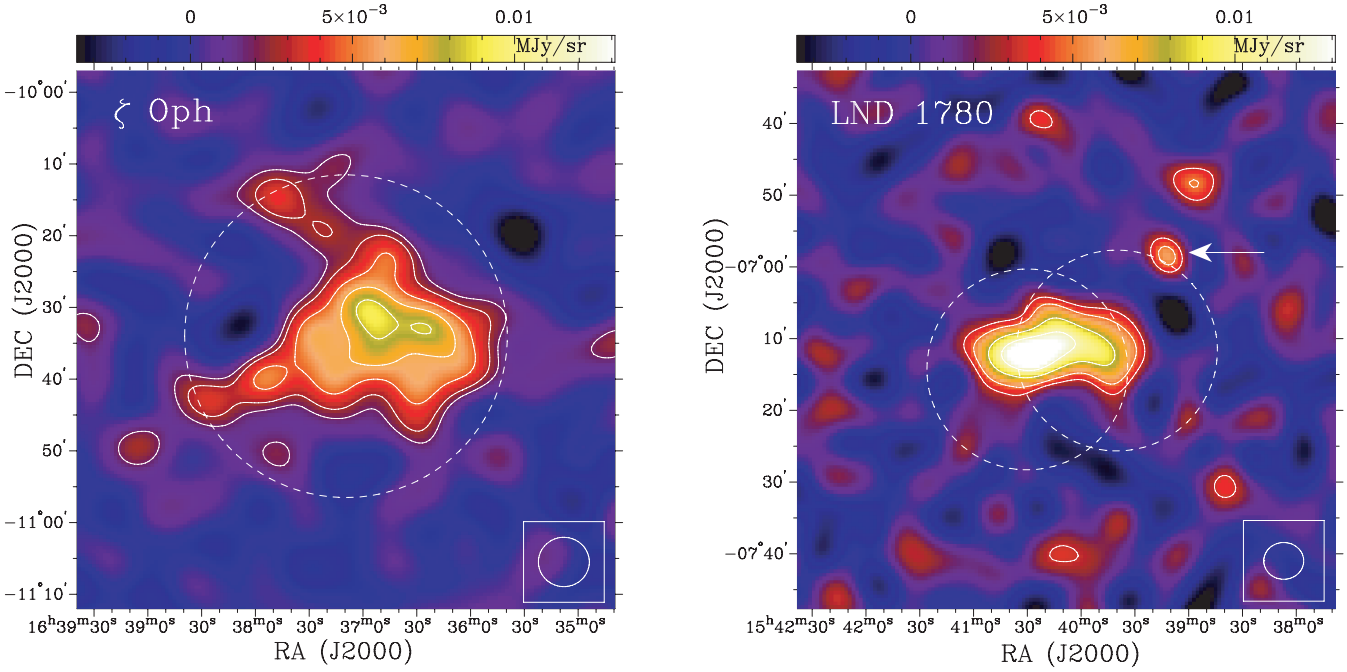

Figure 2. CLEANed 31-GHz images of ζ Oph (left) and LDN 1780 (right). Contours are 10, 30, 50, 70, 90 per cent of the peak brightness, which is 9×10^{-3} MJy sr^{-1} in ζ Oph and 0.016 MJy sr^{-1} in LDN 1780. The FWHM primary beams of CBI1 and CBI2 are shown as dashed lines (in LDN 1780, there are two pointings). These images have not been beam corrected. The point source NVSS 153909-065843 in LDN 1780 is marked with an arrow. The synthesized beam is shown at the bottom right corner of each frame.

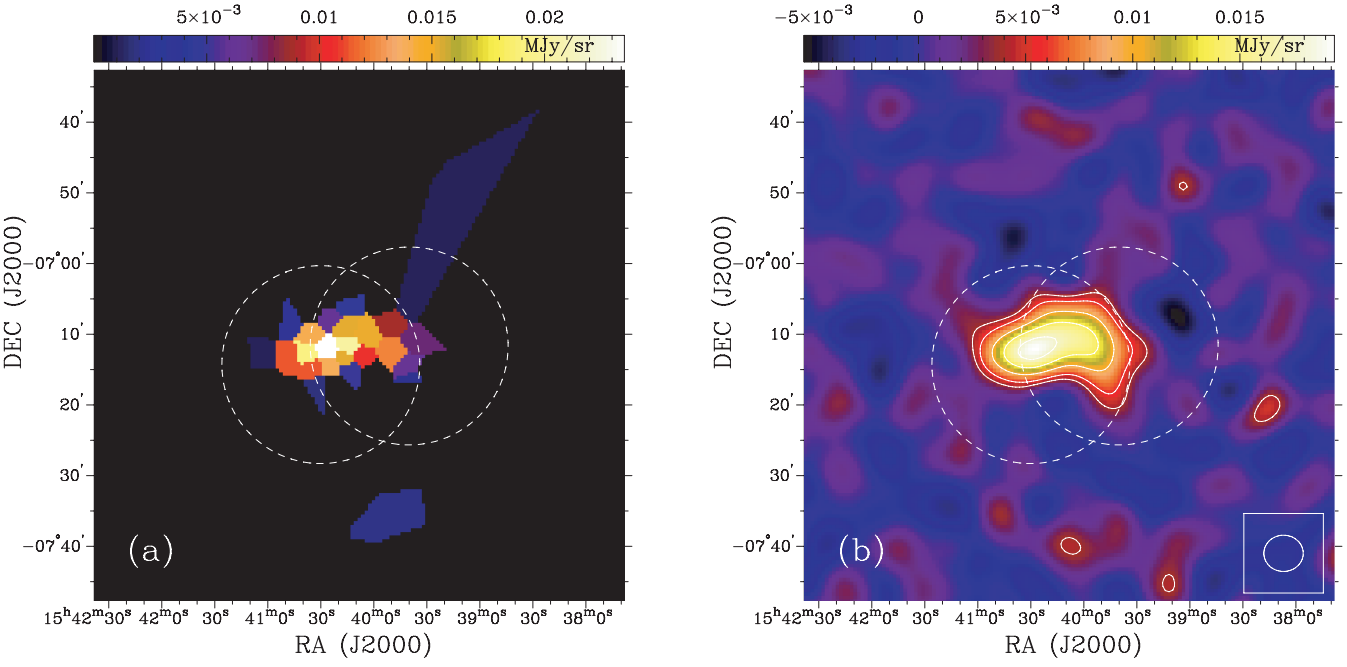

Figure 3. Left: Voronoi model of the visibilities of LDN 1780. This model has 55 polygons. Right: the convolution of the model in the left with the synthetic beam of the data, obtained using natural weights.

dynamic range is larger with the VIR reconstruction: 14.8 versus 11.5 from CLEAN. The disadvantage of the VIR reconstruction is the large amount of CPU time required.

Although the VIR reconstruction is better, both techniques give very similar results. Because of this, we trust the CLEAN reconstruction and used those images for the rest of the investigation.

2.2 Auxiliary data

Table 2 lists the auxiliary data used here. We used images form the Southern H Alpha Sky Survey Atlas (SHASSA), the *Spitzer*, *IRAS*, *ISO*, *COBE* and *WMAP* satellites, and low frequency data from the Parkes-MIT-NRAO (PMN) Survey, the Rhodes/HartRAO Survey,

Table 2. Auxiliary data used.

Survey/Telescope	λ/ν	θ^a	Reference
SHASSA	656.3 nm	0.8 arcmin	Gaustad et al. (2001)
Spitzer[b]	8 μm	2 arcsec	Fazio et al. (2004)
IRAS/IRIS	12, 25, 60 and 100 μm	3.8–4.3 arcmin	Miville-Deschênes & Lagache (2005)
ISO	100 and 200 μm	∼1 arcmin	Kessler et al. (1996)
COBE/DIRBE	100, 140 and 240 μm	∼0.°7	Hauser et al. (1998)
WMAP	23, 33, 41, 61 and 94 GHz	53–13 arcmin	Hinshaw et al. (2009)
PMN	4.85 GHz	∼5 arcmin	Griffith & Wright (1993)
Stockert	2.72 GHz	∼20 arcmin	Reif, Steffen & Reich (1984)
HartRAO	2.326 GHz	∼20 arcmin	Jonas, Baart & Nicolson (1998)
Stockert	1.4 GHz	∼35 arcmin	Reich & Reich (1986)
Parkes	0.408 GHz	51 arcmin	Haslam et al. (1981)

[a] θ is the angular resolution FWHM
[b] Spitzer programme 40154

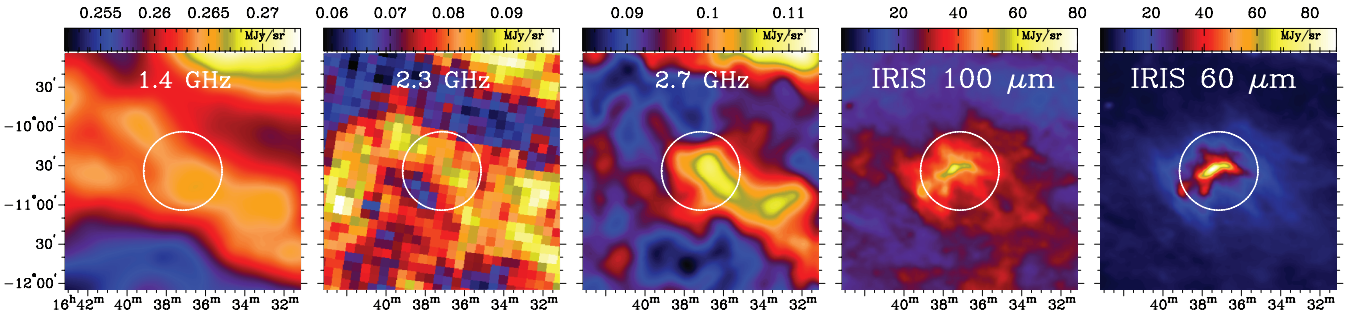

Figure 4. Maps from the auxiliary data around the extraction aperture for ζ Oph, 3° per side, in J2000 equatorial coordinates. The 1° extraction aperture is shown.

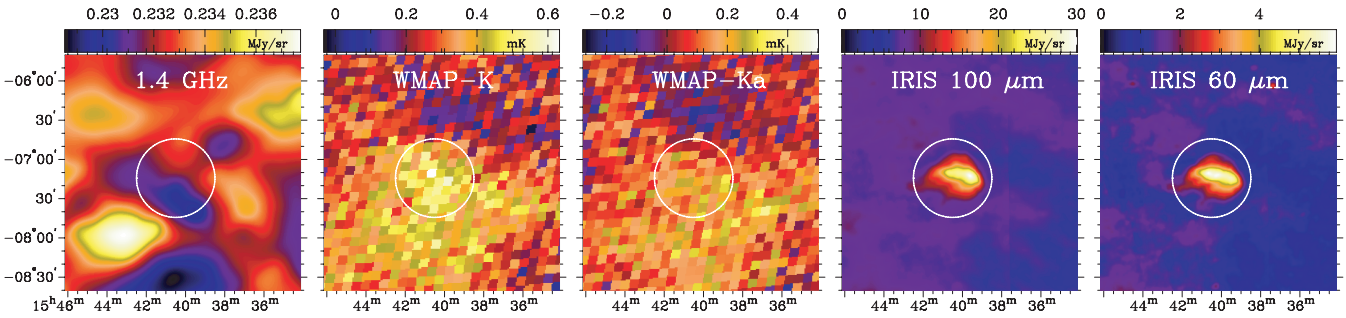

Figure 5. Maps from the auxiliary data around the extraction aperture for LDN 1780, 3° per side, in J2000 equatorial coordinates. The 1° extraction aperture is shown.

the Stockert Radio Telescope and the Haslam 408-MHz Survey. Figs 4 and 5 show large fields of 3° around the two clouds from some of the aforementioned data.

3 ANALYSIS

3.1 Expected radio emission from Hα emission.

The radio free–free emission must be accurately known in order to quantify the contribution of any dust-related excess emission at GHz frequencies. One way to estimate its contribution is with the Hα emission intensity, provided that this line is the result of *in situ* recombination and not scattering by dust.

We used the continuum-corrected Hα image from the SHASSA Survey (Gaustad et al. 2001). On the region of ζ Oph, the image was saturated in the position of the star ζ Oph so reprocessing was necessary to get a smooth image. We masked the saturated pixels and interpolated their values using the adjacent pixels. Then, a median filter was applied to remove the field stars. The processed image was corrected for dust absorption using the $E(B-V)$ template from Schlegel, Finkbeiner & Davis (1998) and the extinction curve given by Cardelli, Clayton & Mathis (1989). The extinction at Hα is $A(\mathrm{H}\alpha) = 0.82\,A(\mathrm{V})$ and using $R_\mathrm{V} = A(V)/E(B-V) = 3.1$ we have that $A(\mathrm{H}\alpha) = 2.54\,E(B-V)$. Finally, we generated a free–free brightness temperature map at 31 GHz using the relationship between Hα intensity and free–free brightness temperature presented in Dickinson, Davies & Davis (2003) assuming a

typical electron temperature $T_e = 7000$ K, appropriate for the solar neighbourhood.

3.2 SED fit

In this analysis we did not use the CBI data because of the large flux loss on angular scales larger than a few times the synthesized beam. We performed simulations to estimate the flux loss after the reconstruction and we could only recover ∼20 per cent of the flux. This would imply that most of the emission from these two clouds is diffuse with respect to the CBI1 and CBI2 beams.

The images were smoothed to a common resolution of 53 arcmin, the lowest resolution of the data used (*WMAP* K). We integrated the auxiliary data in a circular aperture 1° in diameter around the central coordinates of the 31-GHz data. Background emission was subtracted integrating in an adjacent region close to the aperture. This is necessary in the case of the low frequency radio data because these surveys have large baseline uncertainties (see for example Reich & Reich 2009, or the discussion in Davies, Watson & Gutierrez 1996). In Table 3 we present flux densities for ζ Oph and LDN 1780 in this aperture.

3.2.1 ζ Oph

Fig. 6 shows the ζ Oph SED within a 1° aperture, as tabulated in Table 3. The model is the sum of synchrotron, free–free, thermal dust and spinning dust emissions. We used a synchrotron spectral index ($T_b \propto \nu^{\beta_S}$) with $\beta_S = -2.7$ (Davies et al. 1996). The free–free power law is fixed to the predicted brightness temperature at 31 GHz obtained from the Hα image. The spectral index used is $\beta_{ff} = -0.12$ (Dickinson et al. 2003). The dominant source of error in the determination of the free–free emission through the Hα line is the correction for dust absorption. In Fig. 6, the dotted lines denote limits for the free–free law: the lower is the emission expected from the Hα image without dust absorption correction and the upper dotted line is the emission expected with the correction (we assume that all the absorption occurs as a foreground to the Hα emission). A modified blackbody with fixed emissivity index $\beta = 1.6$ and T = 24 K fits the *DIRBE* 240, 140 and 100-μm data points. The spinning dust component was fitted using the Ali-Haïmoud, Hirata & Dickinson (2009) models. The main parameters used in the spinning dust model were $n(H) = 100$ cm^{-3} and a temperature of 30 K. The emissivities are given in terms of the H column density taken to be $N_H = 1.4 \times 10^{21}$cm^{-2} (Morton 1975). The parameters of the dust properties are reasonable for these environments, and were taken from Weingartner & Draine (2001).

On 1° spatial scales, the free–free emission from the H II region dominates the spectrum in the cm range. The angular resolution of the auxiliary radio data is lower than that of the CBI, so we cannot make a flux comparison on the CBI angular scales.

Table 3. Flux densities extracted within a 1° circular aperture for ζ Oph and LDN 1780.

Freq. (GHz)	Telescope/ Survey	θ^a (arcmin)	Flux density ζ Oph (Jy)	Flux density LDN 1780 (Jy)
0.408	Parkes	51	55.4 ± 5.5	39.6 ± 4.0
1.4	Stockert	40	66.9 ± 6.7	56.9 ± 5.7
2.3	HartRAO	20	19.2 ± 1.9	9.5 ± 1.0
2.7	Stockert	20.4	23.7 ± 2.4	14.9 ± 1.4
23	*WMAP*	52.8	7.6 ± 0.1	1.5 ± 0.1
33	*WMAP*	36.6	7.0 ± 0.2	0.9 ± 0.2
41	*WMAP*	30.6	7.0 ± 0.2	0.6 ± 0.2
61	*WMAP*	21	6.2 ± 0.4	<1.0 (3σ)
94	*WMAP*	13.2	7.2 ± 0.6	<2.1 (3σ)
1249	DIRBE	42	4940 ± 580	1600 ± 90
2141	DIRBE	42	7570 ± 300	4150 ± 320
2997	DIRBE	42	5600 ± 200	2900 ± 160

$^a\theta$ is the angular resolution FWHM

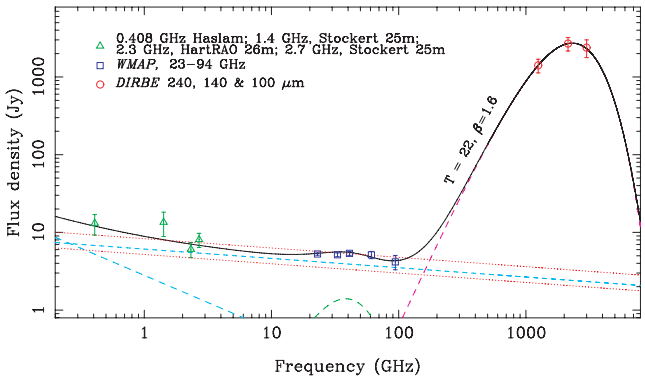

Figure 6. SED of ζ Oph in 1° aperture. The dotted red lines show the maximum and minimum free–free contribution expected given the Hα emission. In green is the spinning dust emission from a model of Ali-Haïmoud et al. (2009).

3.2.2 *Surface brightness spectral comparison*

The PMN image (Fig. 7) has an angular resolution similar to that of the CBI. However this survey has been high-pass filtered; extended emission on scales larger than ∼20 arcmin is removed (Griffith & Wright 1993). To make a comparison on CBI angular scales, we simulated visibilities of the PMN image using the same (u, v) coverage of our CBI data. Since large scale modes have been removed from the PMN data, we exclude visibilities at (u, v) radii < 137

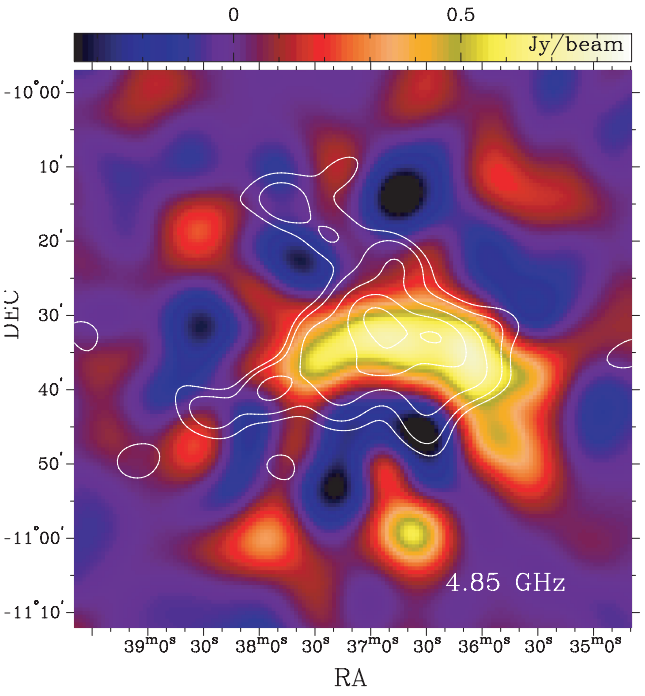

Figure 7. Simulated 4.85-GHz image of ζ Oph from PMN survey. The 33 GHz contours are overlaid.

Table 4. Surface brightness values in the peak of the 31 GHz image.

Frequency (GHz)	Telescope	Surface brightness mJy/beam	Beam size (arcmin)
4.85	Parkes 64 m	11 ± 4	5.1
31	CBI	25 ± 4	7.7

wavelengths (corresponding to angular scales $\gtrsim$25 arcmin). Ideally we should consider only visibilities that correspond to angular scales $\lesssim$15 arcmin to make a conservative analysis, but doing this excludes most of the visibilities resulting in no signal. Table 4 lists the surface brightness values at the peak of the 31-GHz image. The 4.85-/31-GHz spectral index is $\alpha^{31}_{4.85} = 0.43 \pm 0.20$. We see that $\alpha^{31}_{4.85}$ is significantly different (at the 2.75σ level) from -0.12, the spectral index if the emission at 31 GHz were produced by optically thin free–free emission with $T_e \sim 7000$ K. This corresponds to a difference between the 31-GHz intensity and the value expected from a free–free power law fixed to the PMN point, the non free–free specific intensity, of $I^{\rm nff}_{31} = I_{31} - I_{4.85}(4.85/31)^{-0.12} = (12 \pm 5)$ mJy beam^{-1}. The significance of the excess is not very high, but we note that this is a comparison at the peak of the 31-GHz map, which is coincident with the bulk of the free–free emission.

3.2.3 *LDN 1780*

At the location of LDN 1780, the Hα emission present in the SHASSA image is probably scattered light from the Galactic plane (Mattila, Juvela & Lehtinen 2007). Recently, Witt et al. (2010) confirm this result and show that the cloud is embedded in a weaker diffuse Hα background, of which approximately half is due to scattered light. In contrast, del Burgo & Cambrésy (2006) state that the Hα emission is from the cloud itself and suggest a very high rate of cosmic rays to explain the hydrogen ionization. Whichever is the case, we can set an upper limit to the free–free contribution using the SHASSA image. The 100, 140 and 240 μm DIRBE and *WMAP* 94-GHz points were fitted using a modified blackbody with fixed emissivity index $\beta = 2$. The derived temperature is 17 K. For the spinning dust component we used n(H) = 500 cm^{-3} and $T = 20$ K. We estimated the H column density using the extinction map from Schlegel et al. (1998). This estimate used the relation from Bohlin, Savage & Drake (1978) valid for diffuse clouds: $N(\mathrm{H+H_2})/E(B-V) = 5.8 \times 10^{21}$cm^{-2}mag^{-1}. We found $N_{\rm H} = 3.5 \times 10^{21}$cm^{-2}.

Fig. 8 shows the fit. The pair of dotted lines sets limits on the free–free contribution from the Hα data. On the figure are also plotted 3σ upper limits to the contribution at 61 and 94 GHz from the *WMAP* *V* and *W* bands. This SED shows an excess over optically thin free–free emission at cm wavelengths. The spinning dust model is consistent with the SED in a 1° aperture.

3.3 Morphological analysis

If dust is responsible for the 31-GHz emission in these clouds, we expect a morphological correspondence with IR emission. A discussion of the infrared emission from dust can be found in Draine & Li (2007) and references therein. The 100-μm emission is due to grains bigger than 0.01 μm that are in equilibrium with the IRF at a temperature ∼10–20 K. On the other hand, the mid-IR emission traces VSGs at ∼100 K. They are too hot to be in equilibrium with the environment so these grains are heated stochastically by starlight photons and, given the very small heat capacity of a VSG,

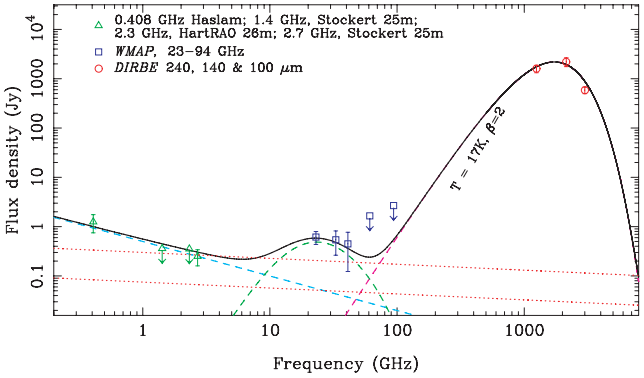

Figure 8. SED of LDN 1780. As in Fig. 6, the red dotted lines show upper and lower limits for the free–free contribution. The symbols with arrows are upper limits (3σ). In green is a spinning dust model from Ali-Haïmoud et al. (2009).

a single UV photon increases the particle temperature enough to emit at $\lambda < 60$ μm.

In the SED of ζ Oph the dominant contribution at 31 GHz is free–free emission. However, inspection of the sky-plane images in Fig. 9 suggests that there is no correspondence between the free–free templates (Fig. 9 a,b) and the 31-GHz contours. The CBI data seem to match better with a combination of free–free and IR emission. We note, however, that the south-eastern arm of the ζ Oph cloud is slightly offset by ∼3 arcmin from its IR counterpart. This offset is larger than the rms pointing accuracy of CBI, of order 0.5 arcmin.

In LDN 1780 there are clear differences among the IR images (Fig. 10). By quantifying these differences we can investigate which kind of dust grains (if big grains or VSGs) are responsible for the 31-GHz emission in this cloud.

3.3.1 *LDN 1780*

3.3.2 *Sky plane correlations*

Here we investigate sky-plane cross-correlations. For this we used MockCBI, a programme which calculates the visibilities $V(u, v)$ of an input image $I_\nu(x, y)$ given a reference (u, v) data set. We computed the visibilities for the IRIS and free–free templates as if they were observed by the CBI with the (u, v) sampling of our data. We reconstructed these visibilities in the same way that we did with the CBI data. Finally, we computed the correlation between the CBI, the IRIS and free–free templates within a square box, 30 arcmin per side, centred at the phase centre of the 31-GHz data.

To estimate the error bars in the correlations, we performed a statistical analysis. We added Gaussian noise to the observed visibilities and reconstructed them 1000 times. Then, we correlated the comparison templates with the noisy mock data set.

The histogram in Fig. 11(a) shows the distribution of the Pearson correlation coefficient of the simulated data. The width of the distribution gives us an estimate of the uncertainty in the correlation coefficients and also in the slope of the linear relation between the IR and 31-GHz data. Fig. 11(b) shows the distribution of the proportionality factor between the emission at 31 GHz and the emission at 100 μm. Table 5 lists the derived parameters. The errors are from the rms dispersion of the Monte Carlo simulations; they are conservative because of the injection of noise to the data.

In the case of ζ Oph, there are no significant differences between the different IR wavelengths and the best correlation is with the free–free template. As we could see in the SED of this cloud (Fig. 6),

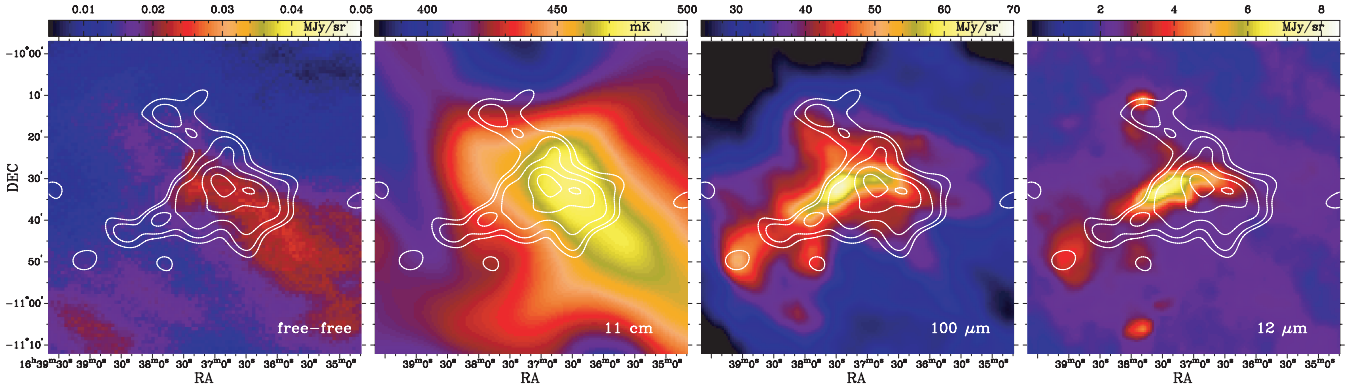

Figure 9. Comparison of different templates of ζ Oph on the sky plane. From the left to right we show the free–free template obtained from the Hα image, the Stockert 2.7-GHz continuum map, the *IRAS* 100-μm map (which traces large dust grains), and the *IRAS* 12-μm map (which traces very small grains). The contours show the CLEANED image of ζ Oph. Contours are as in Fig. 2. The south-eastern 'arm' of the 31-GHz contours has no counterpart in the free–free template; however it resembles the dust emission.

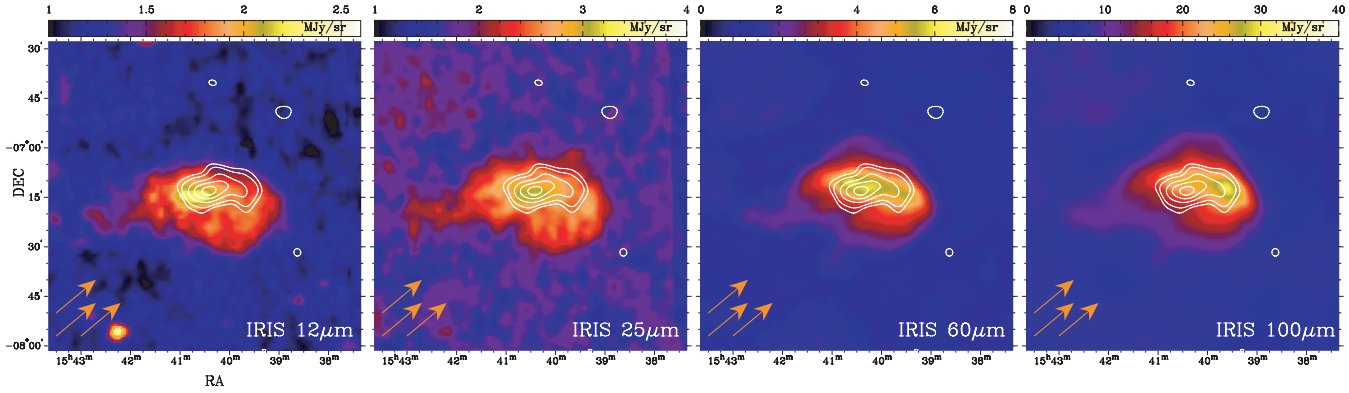

Figure 10. Comparison of the restored CBI2 image of LDN 1780 with *IRAS* templates. The radio point source NVSS 153909-065843 has been subtracted from the CBI2 data. Contours are as in Fig. 2. Note the morphological differences between the *IRAS* bands. The arrows in the corner are perpendicular to the Galactic plane and point towards the north Galactic pole.

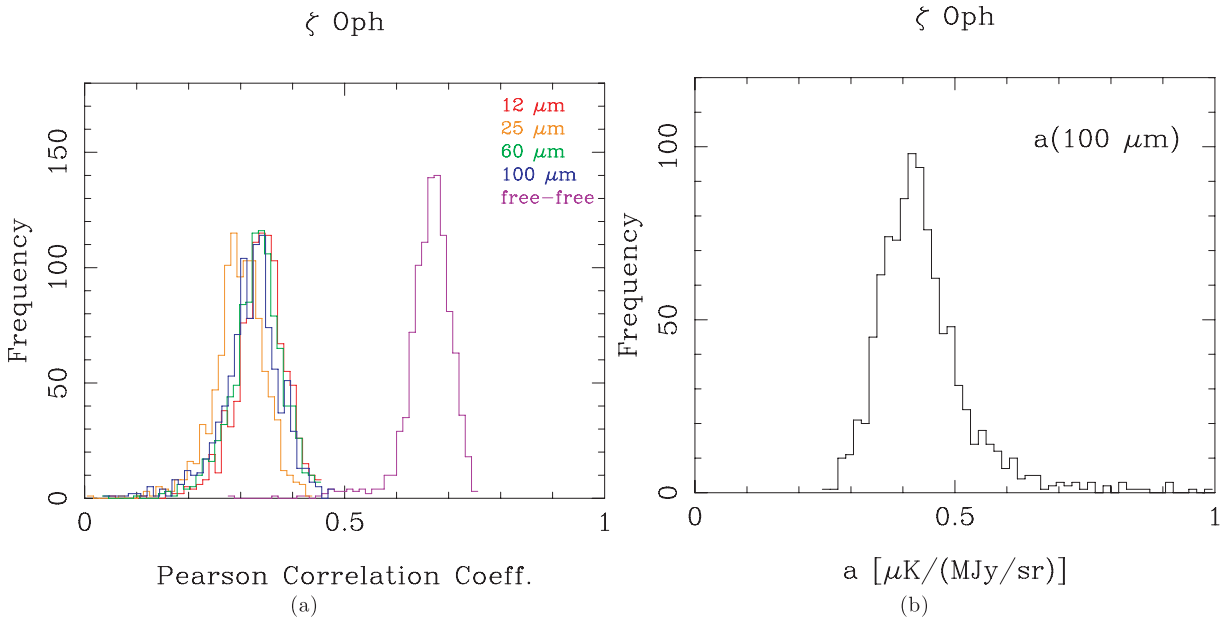

Figure 11. Histograms form the Monte Carlo simulations. Left: histogram of the distribution of the correlation coefficient r for the different templates on ζ Oph. The correlation with the free–free template is significantly better than the correlation with any dust template. Right: histogram of the distribution of a, the proportionality factor between the 31 GHz and the 100-μm images. The rms dispersion of these simulations is used as the error bar for our results.

Table 5. Sky correlation parameters for ζ Oph. r is the linear correlation coefficient and a is the proportionality factor between the 31-GHz image and various templates in units of μK (MJy/sr)$^{-1}$. The errors are given by the dispersion in the Monte Carlo simulations.

	ff	12 μm	25 μm	60 μm	100 μm
r	0.7 ± 0.1	0.5 ± 0.1	0.4 ± 0.1	0.5 ± 0.1	0.4 ± 0.1
a	460 ± 100	2.4 ± 0.5	2.7 ± 0.1	0.2 ± 0.1	0.4 ± 0.1

Table 6. Correlation parameters for LDN 1780. r is the linear correlation coefficient and a is the proportionality factor between the 31-GHz image and various templates in units of μK (MJy/sr)$^{-1}$. The errors are given by the dispersion in the Monte Carlo simulations.

	8 μm	12 μm	25 μm	60 μm	100 μm
r	0.6 ± 0.1	0.5 ± 0.1	0.7 ± 0.05	0.8 ± 0.1	0.6 ± 0.1
a	5.3 ± 1.0	5.2 ± 1.4	3.7 ± 0.9	0.9 ± 0.2	0.2 ± 0.1

most of the radio emission is free–free, so it is not a surprise that the best correlation is with the free–free template.

In LDN 1780, the correlations between 31 GHz and the IR data show more interesting results. Here, all the IR templates correlate better with the CBI data than in ζ Oph. The best match is with *IRAS* 60 μm, as can be inferred qualitatively from Fig. 10; the Monte Carlo simulations confirm this result (Fig. 12a). The emission at 60 μm in the diffuse ISM is mainly from VSGs and a 30–40 per cent contribution from big grains (Desert., Boulanger & Puget 1990) so our results favour a VSGs origin for the cm wave radiation. Table 6 lists the results.

PAH emission at 8 and 12 μm has similar correlation coefficients to that of the 100-μm emission. However, the emission of VSGs depend on the strength of the IRF. The differences in morphology that appear in this cloud depend both on the distribution of grains within the cloud and in the manner that the cloud is illuminated by the IRF. In the next section we investigate how the IRF illuminates this cloud.

3.3.3 *IRF on LDN 1780*

The radio emission from spinning VSGs is fairly independent of the IRF (Draine & Lazarian 1998b; Ali-Haïmoud et al. 2009; Ysard & Verstraete 2010). On the other hand, their near-IR (NIR) emission is due to stochastic heating by interstellar photons so it is proportional to the intensity of the radiation field and to the amount of VSGs. Therefore, NIR templates corrected for the IRF would trace better the distribution of VSGs.

The intensity of the radiation field G_0 can be estimated (as in Ysard et al. 2010) from the temperature of the big grains T_{BG} in the cloud. We constructed a temperature map of those grains fitting a modified blackbody to the *ISO* 100- and 200-μm images pixel-by-pixel (at the same resolution). With this temperature map, we calculated G_0 given that

$$G_0 = \left(\frac{T_{BG}}{17.5\ \mathrm{K}} \right)^{\beta+4}, \quad (1)$$

with $\beta = 2$. We divided the NIR templates (8 and 12 μm) by our G_0 map and then repeated the correlations with the 31-GHz data. Again, to estimate error bars, we used the Monte Carlo simulations. The correlations in this case are tighter than with the uncorrected templates; here $r = 0.69 \pm 0.04$, a 2σ improvement. Fig. 13 shows examples of the correlations in this case.

4 COMPARISON OF 31-GHZ EMISSIVITIES

One motivation for this work is that the physical conditions in translucent clouds approach that of the cirrus clouds. Here, we compare the radio emission of different clouds in terms of their $N(H)$. To avoid differences in beam sizes and frequencies observed, we choose to compare only sources observed by the CBI, at 31 GHz and scales of 4–8 arcmin. We also calculate an averaged column density for the cirrus clouds using the extinction map from Schlegel

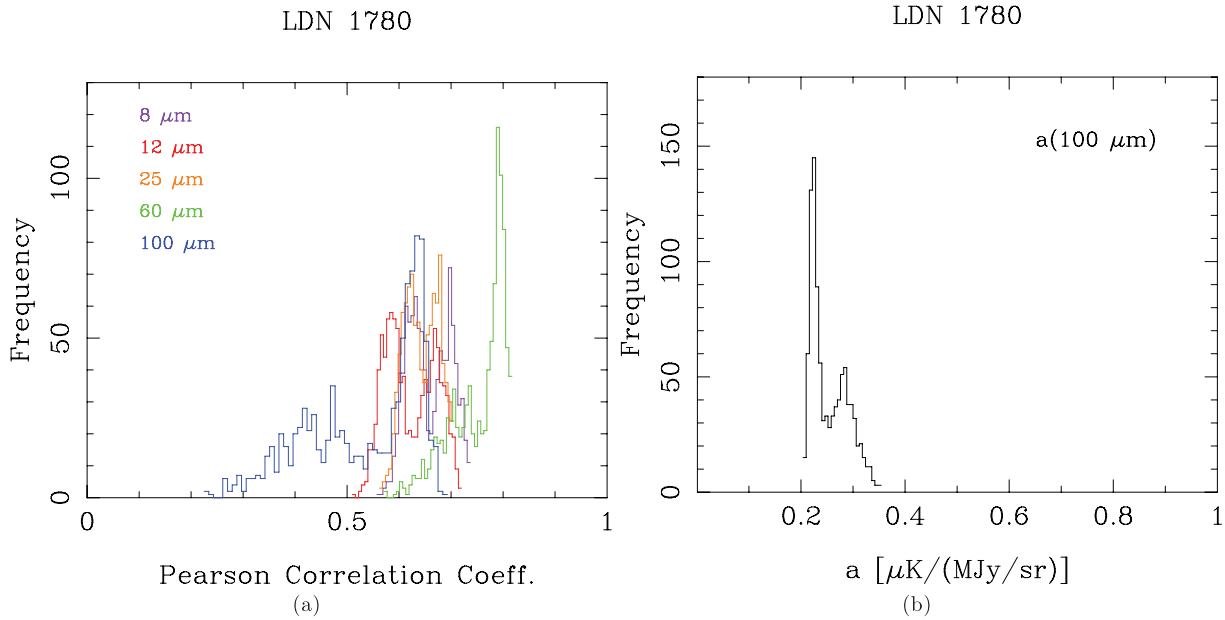

Figure 12. Histograms from the Monte Carlo simulations for LDN 1780. Left: distribution of the correlation coefficient r for the different IR templates. Right: histogram of the distribution of a, the proportionality factor between the 31 GHz and the 100-μm images.

Table 7. Emission parameters for different clouds, all of them but the cirrus were observed by the CBI at 31 GHz. The second column is the column density, the third is the peak intensity at 31 GHz and the fourth is the emissivity at 31 GHz. References are the following: (1) Leitch et al. (1997), (2) Casassus et al. (2006), (3) Casassus et al. (2008), (4) Castellanos et al. (2011).

	$N(H)^a$	$I_{31}{}^b$	$\epsilon_{31}{}^c$
Cirrus[1]	0.15 ± 0.07	6.9 ± 1	4.6 ± 2.0
ζ Oph	0.22 ± 0.02	9 ± 1	4.1 ± 0.6
LDN 1780	0.45 ± 0.04	16 ± 1	3.5 ± 0.4
LDN 1622[2]	1.5 ± 0.15	30 ± 2	2.0 ± 0.2
ρ Oph[3]	5.0 ± 0.50	180 ± 20	3.2 ± 0.5
M78[4]	22.8 ± 0.23	210 ± 30	0.9 ± 0.1

^{a}: $\times 10^{22}$ cm^{-2}
^{b}: $\times 10^{-3}$ MJy sr^{-1}
^{c}: $\times 10^{-24}$ MJy sr^{-1} cm^2

et al. (1998) in the positions observed by Leitch et al. (1997) at frequency of 32 GHz and a beam size ∼7 arcmin. This beam and frequency are similar to those of the CBI.

In Table 7, we list the radio intensity at the peak of the CBI images, alongside a value for the column density at the same position and the ratio between these two quantities. In Fig. 14 we plot these quantities. The linear fit shown has a slope of 0.54 ± 0.10 MJy sr^{-1} cm^{-4} and the correlation coefficient is $r = -0.87$. There seems to be a trend in the direction of diminishing emissivity with increasing column density. Despite the large variations in column density (∼2–3 orders of magnitude), it is interesting that the emissivities of the clouds lie in a small range of ∼1 order of magnitude. However, it is worth noting that *if* the inverse relation we see is real, it will indicate that the anomalous emission is not associated with large dust grains, since their number increases with density, because of dust growth. A similar result was obtained by Lagache (2003), who used *WMAP* data combined with IR templates and gas tracers in the whole sky on angular scales of 7°.

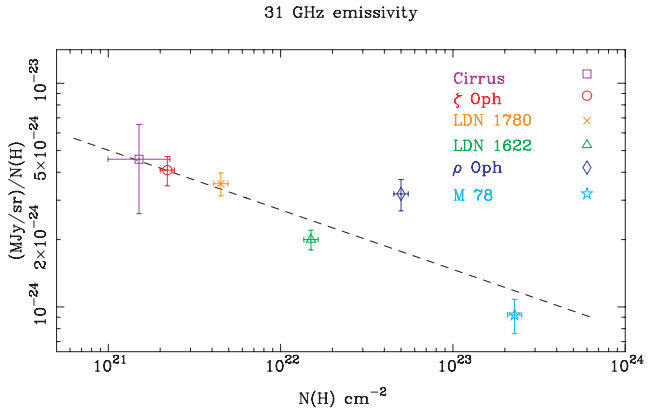

Figure 14. Emissivity at 31 GHz versus column density for different clouds observed with the CBI. The point corresponding to cirrus clouds was obtained as an average from the results of Leitch et al. (1997). The dashed line is the best linear fit to the data.

5 CONCLUSIONS

We have presented 31-GHz data for two translucent clouds, ζ Oph and LDN 1780, with the aim of characterizing their radio emissivities. We found an anomalous emission excess in both clouds at 31 GHz on angular scales of ∼7 arcmin in ζ Oph and ∼5 arcmin in LDN 1780.

The SED of ζ Oph on large (1°) angular scales is dominated by free–free emission from the associated H II. Because of this, it is difficult to quantify the contribution from dust to the 31-GHz data. However, when comparing with the optically thin free–free extrapolated from the 5-GHz PMN image, we find a 2.4 σ excess in surface brightness at 31 GHz on spatial scales of 7 arcmin in surface brightness.

In the SED of LDN 1780 we also see an excess on 1° angular scales. The free–free contribution in this cloud is expected to be

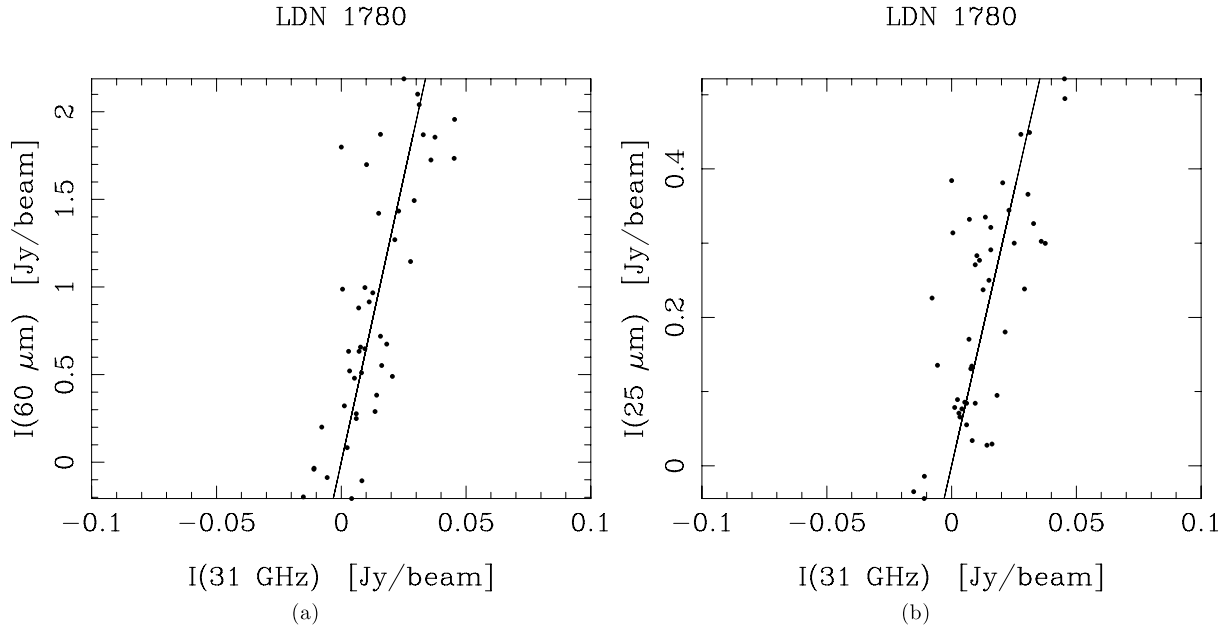

Figure 13. Pixel-by-pixel correlation of CBI data with *IRAS* 60 μm and the corrected *IRAS* 25-μm templates on LDN 1780. *IRAS* 60 μm correlates better in the more diffuse regions while IRAC 25 μm does better in the peak of the CBI image.

very low; the Hα emission may be scattered light from the IRF, so it would not have a radio counterpart. A spinning dust component can explain the anomalous emission excess in the SED. Correlations between the cm wave data and IR-templates shows a trend favouring *IRAS* 25 and 60 μm. The best match in this case is with *IRAS* 60 μm although the peak of the CBI image is best matched by IRAC 8 μm. We corrected the IRAC 8 μm and *IRAS* 12 μm by the IRF and found a tighter correlation with these corrected templates. In the spinning dust models, the VSGs dominate the radio emission. Our results support this mechanism as the origin for the anomalous emission in this cloud.

The 31-GHz emissivities found in both clouds are similar and have intermediate values between the cirrus clouds and the dark clouds. The emissivity variations with column density are small, although we find an indication of an inverse relationship, which would further support a VSGs origin for the cm emission. The anomalous foreground which contaminates CMB data comes from cirrus clouds at typically high Galactic latitudes. Here, we see that there is not a large difference between the radio emissivity of cirrus and translucent clouds on 7 arcmin angular scales. Because of this similarity, translucent clouds are good places to investigate the anomalous CMB foreground.

ACKNOWLEDGMENTS

We are most grateful to Mika Juvela who kindly shared with us the LDN 1780 *ISO* images. We thank an anonymous referee for a thorough reading and very useful comments. MV acknowledges the funding from Becas Chile. SC acknowledges support from a Marie Curie International Incoming Fellowship (REA-236176), from FONDECYT grant 1100221, and from the Chilean Center for Astrophysics FONDAP 15010003. CD acknowledges an STFC Advanced Fellowship and ERC grant under FP7. LB and RB acknowledge support from CONICYT project Basal PFB-06. This work has been carried out within the framework of a NASA/ADP ROSES-2009 grant, n. 09-ADP09-0059. The CBI was supported by NSF grants 9802989, 0098734 and 0206416, and a Royal Society Small Research Grant. We are particularly indebted to the engineers who maintained and operated the CBI: Cristóbal Achermann, José Cortés, Cristóbal Jara, Nolberto Oyarace, Martin Shepherd and Carlos Verdugo. This work was supported by the Strategic Alliance for the Implementation of New Technologies (SAINT – see www.astro.caltech.edu/chajnantor/saint/index.html) and we are most grateful to the SAINT partners for their strong support. We gratefully acknowledge support from the Kavli Operating Institute and thank B. Rawn and S. Rawn Jr. We acknowledge the use of the Legacy Archive for Microwave Background Data Analysis (LAMBDA). Support for LAMBDA is provided by the NASA Office of Space Science. We used data from the Southern H-Alpha Sky Survey Atlas (SHASSA), which is supported by the National Science Foundation.

REFERENCES

Ali-Haïmoud Y., Hirata C. M., Dickinson C., 2009, MNRAS, 395, 1055
Ami Consortium et al., 2009, MNRAS, 394, L46
Bennett C. L. et al., 2003, ApJS, 148, 97
Black J. H., Dalgarno A., 1977, ApJS, 34, 405
Bohlin R. C., Savage B. D., Drake J. F., 1978, ApJ, 224, 132
Boulanger, F., Perault M., 1988, ApJ, 330, 964
Cabrera G. F., Casassus S., Hitschfeld N., 2008, ApJ, 672, 1272
Cardelli J. A., Clayton G. C., Mathis J. S., 1989, ApJ, 345, 245
Casassus S., Cabrera G. F., Förster F., Pearson T. J., Readhead A. C. S., Dickinson C., 2006, ApJ, 639, 951
Casassus S. et al., 2008, MNRAS, 391, 1075
Castellanos P. et al., 2011, MNRAS, 411, 1137
Condon J. J., Cotton W. D., Greisen E. W., Yin Q. F., Perley R. A., Taylor G. B., Broderick J. J., 1998, AJ, 115, 1693
Davies R. D., Watson R. A., Gutierrez C. M., 1996, MNRAS, 278, 925
del Burgo C., Cambrésy L., 2006, MNRAS, 368, 1463
de Oliveira-Costa A., Tegmark M., Davies R. D., Gutiérrez C. M., Lasenby A. N., Rebolo R., Watson R. A., 2004, ApJ, 606, L89
Desert F.-X., Boulanger F., Puget J. L., 1990, A&A, 237, 215
Dickinson C., Davies R. D., Davis R. J., 2003, MNRAS, 341, 369
Dickinson C. et al., 2009, ApJ, 690, 1585
Draine B. T., Lazarian A., 1998a, ApJ, 494, L19
Draine B. T., Lazarian A., 1998b, ApJ, 508, 157
Draine B. T., Lazarian A., 1999, ApJ, 512, 740
Draine B. T., Li A., 2007, ApJ, 657, 810
Fazio G. G. et al., 2004, ApJS, 154, 10
Finkbeiner D. P., 2004, ApJ, 614, 186
Finkbeiner D. P., Langston G. I., Minter A. H., 2004, ApJ, 617, 350
Franco G. A. P., 1989, A&A, 223, 313
Gaustad J. E., McCullough P. R., Rosing W., Van Buren D., 2001, PASP, 113, 1326
Griffith M. R., Wright A. E., 1993, AJ, 105, 1666
Haslam C. G. T., Klein U., Salter C. J., Stoffel H., Wilson W. E., Cleary M. N., Cooke D. J., Thomasson P., 1981, A&A, 100, 209
Hauser M. G. et al., 1998, ApJ, 508, 25
Hill R. S. et al., 2009, ApJS, 180, 246
Hinshaw G. et al., 2009, ApJS, 180, 225
Högbom J. A., 1974, A&AS, 15, 417
Jonas J. L., Baart E. E., Nicolson G. D., 1998, MNRAS, 297, 977
Kessler M. F. et al., 1996, A&A, 315, L27
Kogut A., Banday A. J., Bennett C. L., Gorski K. M., Hinshaw G., Reach W. T., 1996a, ApJ, 460, 1
Kogut A., Banday A. J., Bennett C. L., Gorski K. M., Hinshaw G., Smoot G. F., Wright E. I., 1996b, ApJ, 464, L5
Lagache G., 2003, A&A, 405, 813
Leitch E. M., Readhead A. C. S., Pearson T. J., Myers S. T., 1997, ApJ, 486, L23
Low F. J. et al., 1984, ApJ, 278, L19
Magnani L., Blitz L., Mundy L., 1985, ApJ, 295, 402
Mattila K., Juvela M., Lehtinen K., 2007, ApJ, 654, L131
Miville-Deschênes M.-A., Boulanger F., Joncas G., Falgarone E., 2002, A&A, 381, 209
Miville-Deschênes M.-A., Lagache G., 2005, ApJS, 157, 302
Morton D. C., 1975, ApJ, 197, 85
Padin S. et al., 2002, PASP, 114, 83
Pearson T. J. et al., 2003, ApJ, 591, 556
Perryman M. A. C. et al., 1997, A&A, 323, L49
Readhead A. C. S. et al., 2004a, ApJ, 609, 498
Readhead A. C. S. et al., 2004b, Sci, 306, 836
Reich W., Reich P., 2009, in Strassmeier K. G., Kosovichev A. G., Beckman J. E., eds, Proc. IAU Symp. Vol. 259, Cosmic Magnetic fields: From Planets, to Stars and Galaxies. p. 603
Reich P., Reich W., 1986, A&AS, 63, 205
Reif K., Steffen P., Reich W., 1984, Kleinheubacher Berichte, 27, 295
Ridderstad M., Juvela M., Lehtinen K., Lemke D., Liljeström T., 2006, A&A, 451, 961
Schlegel D. J., Finkbeiner D. P., Davis M., 1998, ApJ, 500, 525
Shepherd M. C., 1997, Astron. Data Analysis Software Syst. VI, 125, 77
Snow T. P., McCall B. J., 2006, ARA&A, 44, 367
Stark R., 1990, A&A, 230, L25
Stark R., Dickey J. M., Burton W. B., Wennmacher A., 1994, A&A, 281, 199
Turner B. E., 1994, in Cutri R. M., Latter W. B., eds, ASP Conf. Ser. Vol. 58, The First Symposium on the Infrared Cirrus and Diffuse Interstellar Clouds. Astron. Soc. Pac., San Francisco, p. 307

van Dishoeck E. F., Black J. H., 1986, ApJS, 62, 109
Viala Y. P., Roueff E., Abgrall H., 1988, A&A, 190, 215
Watson R. A., Rebolo R., Rubiño-Martín J. A., Hildebrandt S., Gutiérrez C. M., Fernández-Cerezo S., Hoyland R. J., Battistelli E. S., 2005, ApJ, 624, L89
Weingartner J. C., Draine B. T., 2001, ApJ, 548, 296
Witt A. N., Gold B., Barnes F. S., DeRoo C. T., Vijh U. P., Madsen G. J., 2010, ApJ, 724, 1551
Ysard N., Verstraete L., 2010, A&A, 509, A12
Ysard N., Miville-Deschênes M. A., Verstraete L., 2010, A&A, 509, L1

This paper has been typeset from a TEX/LATEX file prepared by the author.